

# G2L: From Giga-Scale to Cancer-Specific Large-Scale Pathology Foundation Models via Knowledge Distillation

Yesung Cho<sup>1</sup>, Sungmin Lee<sup>2</sup>, Geongyu Lee<sup>1</sup>, Minkyung Lee<sup>2</sup>, Jongbae Park<sup>3</sup>, Dongmyung Shin<sup>1†</sup>

<sup>1</sup>OmixAI Co. Ltd., Seoul, South Korea

<sup>2</sup>RadiSen Co. Ltd., Seoul, South Korea

<sup>3</sup>Kyunghee University, Seoul, South Korea

<sup>1</sup>{yscho, gglee, shinsae11}@omixai.com, <sup>2</sup>{smlee, mkleee317}@radisentech.com, <sup>3</sup>jb@khu.ac.kr

†Corresponding author

## Abstract

Recent studies in pathology foundation models have shown that scaling training data, diversifying cancer types, and increasing model size consistently improve their performance. However, giga-scale foundation models, which are trained on hundreds of thousands of slides covering tens of cancer types and contain billions of parameters, pose significant challenges for practical use due to their tremendous computational costs in both development and deployment. In this work, we present a novel strategy, named the G2L framework, to increase the performance of large-scale foundation models, which consist of only 15% of the parameters of giga-scale models, to a comparable performance level of giga-scale models in cancer-specific tasks. Our approach applies knowledge distillation, transferring the capabilities of a giga-scale model to a large-scale model, using just 1K pathology slides of a target cancer (e.g., breast, prostate, etc.). The resulting distilled model not only outperformed state-of-the-art models of the same size (i.e., large-scale) across several benchmarks but also, interestingly, surpassed the giga-scale teacher and huge-scale models in some benchmarks. In addition, the distilled model exhibited a higher robustness index, indicating improved resilience to image variations originating from multiple institutions. These findings suggest that the proposed distillation approach for a large-scale model is a data- and parameter-efficient way to achieve giga-scale-level performance for cancer-specific applications without prohibitive computational burden.

## Introduction

Foundation models (FMs) have been increasingly adopted in computational pathology to extract morphological features from whole-slide images (WSIs). Especially, vision transformers (ViTs) trained with contrastive learning (Chen et al. 2020; He et al. 2020; Caron et al. 2021; Oquab et al. 2023) or masked image modeling (He et al. 2022; Zhou et al. 2022) have achieved remarkable performance across various downstream applications, such as tumor classification (Brancati et al. 2022; Spanhol et al. 2015) and gene mutation detection (Qu et al. 2021).

Recent studies have shown that scaling the amount of training data, diversifying cancer types, and increasing model size consistently improve the performance of FMs

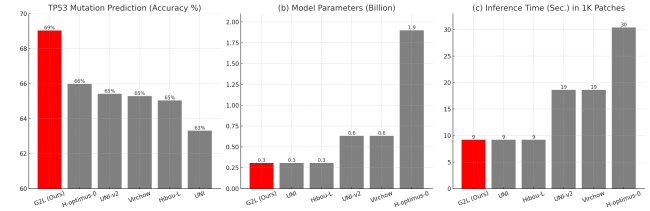


Figure 1: Comparison of G2L-distilled and other foundation models in TP53 mutation prediction benchmark measured by accuracy with model parameters (in billion) and inference times (in seconds). The G2L-optimized model outperforms the others in all metrics, as highlighted in red.

(Zimmermann et al. 2024; Filiot et al. 2024). For instance, giga-scale FMs, such as H-optimus-0 (Saillard et al. 2024) and GigaPath (Xu et al. 2024), employ a ViT-Giga (ViT-G) backbone network with 1.9B parameters (Dosovitskiy et al. 2021) and are trained on hundreds of thousands of pathology slides (e.g., 170K slides for GigaPath) that cover a wide range of cancer types (e.g., 28 types for GigaPath). Consequently, the giga-scale models outperform their smaller-parameter counterparts, such as ViT-Huge (ViT-H) models with 0.6B and ViT-Large (ViT-L) models with 0.3B parameters, in a variety of downstream tasks.

However, the computational demands of giga-scale FMs, which exceed a billion parameters and require hundreds of thousands of slides for training, present significant challenges for both model development and deployment. In particular, these resource-intensive requirements can limit accessibility in research institutions and clinical settings without a scalable computing infrastructure. In addition, while giga-scale FMs serve as a general feature extractor across various types of cancer, they can possibly dilute critical morphological signals specific to a certain cancer due to their significant heterogeneity (Zhao et al. 2025; Weigelt, Geyer, and Reis-Filho 2010). For example, architectural patterns, nuclear morphology, and stromal interactions unique to breast carcinoma (Weigelt, Geyer, and Reis-Filho 2010) may be underrepresented when training data are dominated by other cancers. As a result, its performance can possibly be degraded for fine-grained discrimination within a specific cancer morphology.

To circumvent these challenges, we propose a novel giga-to-large (G2L) distillation framework to improve the performance of a large-scale FM to a comparable level of performance to a giga-scale FM via knowledge distillation. By G2L, a large-scale FM is optimized in a way to increase its sensitivity to a target cancer domain using only 1K pathology slides.

In both breast and prostate cancers, we have evaluated the proposed G2L-distilled model against not only other large-scale FMs but also huge- and giga-scale counterparts across a wide range of downstream tasks, such as gene mutation prediction (Qu et al. 2021), tumor grade classification (Arvaniti et al. 2018), and immune infiltration detection (Saltz et al. 2018; Abousamra et al. 2022). Our results showed that the distilled model outperformed existing large-scale FMs and even surpassed some huge- and giga-scale FMs in a set of benchmarks. These findings demonstrate that the proposed approach is a data- and parameter-efficient method to develop a high-performance, cancer-specific large-scale FM. Fig. 1 compares the G2L-distilled and other FMs based on the TP53 mutation prediction accuracy, model sizes, and inference times, showcasing its superiority over the others.

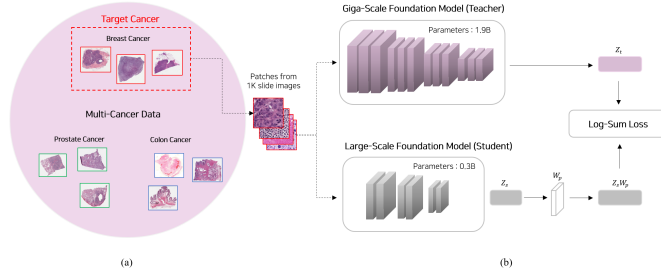


Figure 2: Overview of G2L framework.

## G2L Framework

### Overview

Fig. 2 illustrates the proposed G2L framework to build a cancer-specific, large-scale FM via knowledge distillation. First, a single cancer type that we want to target for the distillation (i.e., target cancer) is chosen in multi-cancer database (e.g., the cancer genome atlas (TCGA) (Weinstein et al. 2013)). Then, we select 1K pathology slides of the target cancer, where each of these slides is divided into a set of patches in the foreground tissue regions (Lee 2025) (Fig. 2a). Finally, we distilled the knowledge of a giga-scale FM as a teacher to a large-scale FM as a student (Miles and Mikolajczyk 2024) (Fig. 2b).

### Implementation Details

For target cancers, we selected popular cancer types that are easily accessible in the public: breast and prostate. More precisely, we used non-overlapping patches with a size of 256 by 256 from 1K pathology slides (40x magnification) in TCGA-BRCA or TCGA-PRAD (Weinstein et al. 2013), where each patch was randomly cropped to a size of 224

by 224 for training. We applied data augmentation to each patch before feeding it to teacher and student FMs, including horizontal/vertical flipping (50% chance), color jittering (50% chance; brightness = 0.15, contrast = 0.15, saturation = 0.1, and hue = 0.05), and Gaussian blurring (10% chance; kernel size = 9 x 9).

For giga- and large-scale FMs, H-optimus-0 (Saillard et al. 2024) (ViT-G/14 with 1.9B parameters), which has reported state-of-the-art performance in many downstream tasks in various cancers, was used as a teacher, and Hibou-L (Nechaev, Pchelnikov, and Ivanova 2024) (ViT-L/14 with 0.3B parameters) was utilized as a student. Since these two FMs have different dimensions of output embeddings (1536 for H-optimus-0 and 1024 for Hibou-L), to match them with each other, we simply attached a linear projection layer with batch normalization at the end of the student network, following (Miles and Mikolajczyk 2024). Finally, the loss function (i.e., Log-Sum Loss in Fig. 2) is defined as follows:

$$D(Z_s, Z_t; W_p) = \log \sum_i |Z_s W_p - Z_t|_i^\alpha \quad (1)$$

where  $Z_s$  and  $Z_t$  are feature vectors of the student and teacher networks, respectively,  $W_p$  is a linear project layer, and  $\alpha$  is a smoothing factor (= 4).

### Hyperparameters and Computing Environment

The training batch size was 32. We used an AdamW optimizer (Kingma and Ba 2015) with an initial learning rate of  $1 \times 10^{-4}$  and a weight decay of 0.05. Both the learning rate and the weight decay followed a cosine annealing schedule, decaying from  $1 \times 10^{-4}$  to  $1 \times 10^{-6}$  and from 0.05 to 0.5, respectively. We stopped distillation training when the current loss value exceeded the average loss value of the last 100 iterations more than 10 times. The computing environment was: three NVIDIA RTX A6000 GPUs, AMD Ryzen Threadripper PRO 3955WX CPU, and 506GB RAM.

## Experiments

### Feature Similarity Before / After G2L

We first investigated whether the student model learns a feature space similar to that of the teacher model after applying the G2L framework. To quantify the similarity, we employed centered kernel alignment (CKA) (Kornblith, Shlens, and Hinton 2019), which measures how similarly two models capture spatial information in their feature embeddings by computing the covariance between them and then normalizing the result to produce a similarity score between 0 and 1, where values closer to 1 indicate higher similarity.

To evaluate how the feature similarity changes before and after G2L, we used patches from two benchmark datasets, BRCAS and BreakHis (see details below). These patches were inferred by the teacher model (H-optimus-0) and the student model (Hibou-L), respectively. The resulting features were then used to compute CKA values, allowing us to assess the degree of spatial alignment in the latent space for each dataset.

## Downstream Task Benchmark

To evaluate the performance of FMs as a general feature extractor without fine-tuning, we first adopted the non-training benchmark method similar to (Cappadona et al. 2024). Concretely, we extracted 50-dimensional image feature vectors using principal component analysis and measured the performance based on the majority vote of the labels (e.g., tumor-infiltrated or not) of the features of  $k$ -nearest neighbors ( $k = 15$ ). For each downstream benchmark, a 10-fold cross-validation was performed. Here, the training data were not used to fine-tune the FMs but only to assign neighbor labels, thereby enabling a purely non-learnable evaluation of embedding quality.

To complement the non-parametric evaluation, we also performed a linear probing (LP) benchmark (Ding et al. 2025; Li et al. 2025), assessing the adaptability of the extracted representations of FMs for lightweight supervision. We trained a linear classifier on top of the frozen FM features using a 6:2:2 data split (train:validation:test). While the non-training method evaluates the intrinsic discriminative structure of features, this LP analysis verifies whether representations effectively support downstream tasks with minimal supervision.

For patch-level downstream benchmarks (e.g., TILS dataset below), each patch was fed into the FMs to extract image features, and the performance was measured accordingly. For slide-level and region-of-interest(ROI)-level downstream tasks (e.g., TP53 dataset below), non-overlapping patches from each slide or ROI were fed into the FMs to extract a set of features, which were then mean-pooled to generate an aggregated slide-level or ROI-level representation.

All downstream benchmarks were either binary or multi-label classification tasks. In the non-training evaluation, we reported performance using accuracy. In the linear-probing benchmarks, we measured AUCs for binary tasks and one-vs-rest macro AUCs for multi-label classification.

For comparison, we have benchmarked not only the original teacher (H-optimus-0 (Saillard et al. 2024)) and student (Hibou-L (Nechaev, Pchelnikov, and Ivanova 2024)) models but also other FMs with large- and huge-scales, including UNI (ViT-L with 307M parameters), UNI-v2 (ViT-H with 632M parameters) (Chen et al. 2024), and Virchow (ViT-H with 632M parameters) (Vorontsov et al. 2023).

**TILS (Tumor-Infiltrating Lymphocytes)** is a patch-level benchmark dataset extracted from the TCGA cohort (Saltz et al. 2018). It contains 5,245 patches of breast cancer, where each patch is annotated as binary labels (i.e., tumor-infiltrating lymphocytes or not).

**TP53** is a slide-level benchmark dataset derived from the TCGA breast cancer cohort (Qu et al. 2021). We randomly sampled 511 slides out of a total of 1,133 slides for the benchmark, excluding any slides used for G2L. The binary label for each slide is TP53-mutation or not.

**IDC (Invasive Ductal Carcinoma)** is a patch-level benchmark dataset that comprises 162 breast cancer slides collected at Radboud University Medical Center

(Janowczyk and Madabhushi 2016). The total number of patches is 277,524, labeled as IDC-positive or IDC-negative.

**BRCAS (Breast Carcinoma Subtyping)** is an ROI-level benchmark dataset that contains 4,537 ROIs of 547 pathology slides from 189 breast cancer patients (Brancati et al. 2022). The label for each ROI covers seven subtypes: normal, benign, usual ductal hyperplasia, flat epithelial atypia, atypical ductal hyperplasia, ductal carcinoma in situ, and invasive carcinoma.

**BreakHis** is an ROI-level benchmark dataset consisting of 7,909 ROIs from 82 slides (24 benign, 58 malignant) collected at the Universidade Federal do Paraná in Brazil (Spanhol et al. 2015). The labels of benign ROIs include adenosis, fibroadenoma, phyllodes tumor, and tubular adenoma whereas the labels of malignant ROIs were ductal carcinoma, lobular carcinoma, mucinous carcinoma, and papillary carcinoma. The dataset provides each ROI image at four magnifications (40 $\times$ , 100 $\times$ , 200 $\times$ , and 400 $\times$ ), enabling comprehensive evaluation across multiple fields of views.

**Gleason** is a patch-level benchmark dataset that includes 77,364 patches of 331 tissue microarray (TMA) core images collected at the Vancouver Prostate Centre (Arvanit et al. 2018). For patch extraction, each TMA image was divided into non-overlapping patches with a size of 256 by 256, and each patch was assigned a label according to the majority vote of annotations from six pathologists. The labels for each patch comprise four categories: benign, Gleason grade 3, grade 4, and grade 5.

**AGGC** is a patch-level benchmark dataset that has 156,130 patches from 150 prostatectomy and 53 biopsy slides collected at Singapore’s National University Hospital (NUH) (Huo et al. 2022). As similar as the Gleason benchmark, we assigned a label of each patch based on the majority class of annotations as five categories: benign, stroma, and Gleason grade 3, grade 4, and grade 5.

**CHIMERA** is a slide-level benchmark dataset that incorporates 190 slides from 95 patients collected from several institutions, including Radboud University Medical Center (Chia et al. 2025). Each slide was labeled as biochemical recurrence positive or negative.

Table 1: Feature similarity measured by CKA values between teacher (H-optimus-0) and student (Hibou-L) models before and after applying G2L framework. The highest value of each row is highlighted in **bold**.

Dataset	CKA before G2L	CKA after G2L
BRCAS	$0.7594 \pm 0.014$	<b><math>0.9683 \pm 0.011</math></b>
BreakHis 40 $\times$	$0.8909 \pm 0.003$	<b><math>0.9558 \pm 0.001</math></b>
BreakHis 100 $\times$	$0.9147 \pm 0.002$	<b><math>0.9686 \pm 0.001</math></b>
BreakHis 200 $\times$	$0.9230 \pm 0.001$	<b><math>0.9734 \pm 0.000</math></b>
BreakHis 400 $\times$	$0.8995 \pm 0.003$	<b><math>0.9575 \pm 0.000</math></b>

Table 2: Benchmark results of existing foundation models of different sizes and the proposed G2L-distilled model. We evaluate accuracy in non-training method (**Top**) and AUC in linear probing (**Bottom**). The best performance is highlighted in **bold**, and the second-best is in underline. \*: evaluated based on binary labels (benign or malignant) and averaged over multiple magnifications. \*\*: evaluated based on sub-typing labels (e.g., adenosis, fibroadenoma, etc.) and averaged over multiple magnifications.

Benchmark	Cancer	H-optimus-0 (ViT-G; 1.9B)	UNI-v2 (ViT-H; 0.6B)	Virchow (ViT-H; 0.6B)	Hibou-L (ViT-L; 0.3B)	UNI (ViT-L; 0.3B)	G2L (Ours) (ViT-L; 0.3B)
<i>Non-training Method (Accuracy)</i>							
TILS	Breast	<u>0.9344 ± 0.006</u>	0.9291 ± 0.007	0.8900 ± 0.007	0.9214 ± 0.008	0.9334 ± 0.007	<b>0.9362 ± 0.005</b>
TP53	Breast	<u>0.6598 ± 0.040</u>	0.6542 ± 0.050	0.6528 ± 0.030	0.6504 ± 0.030	0.6331 ± 0.020	<b>0.6904 ± 0.050</b>
IDC	Breast	0.9141 ± 0.0003	0.9165 ± 0.0003	0.8813 ± 0.0004	0.9074 ± 0.0003	<u>0.9224 ± 0.0003</u>	<b>0.9232 ± 0.0001</b>
BRCA	Breast	<u>0.4526 ± 0.030</u>	<b>0.4638 ± 0.020</b>	0.3677 ± 0.03	0.4103 ± 0.040	0.4305 ± 0.040	0.4520 ± 0.040
BreakHis (Bin.)*	Breast	<b>0.8892</b>	0.8742	0.8102	0.8393	0.8718	<u>0.8841</u>
BreakHis (Sub.)**	Breast	0.5259	<b>0.5502</b>	0.4040	0.4660	0.5105	<u>0.5319</u>
Gleason	Prostate	<b>0.8994 ± 0.002</b>	0.8678 ± 0.003	0.6162 ± 0.003	0.8124 ± 0.002	0.8798 ± 0.002	<u>0.8988 ± 0.001</u>
AGGC	Prostate	<u>0.9226 ± 0.001</u>	0.9170 ± 0.001	0.7540 ± 0.002	0.8788 ± 0.001	0.9194 ± 0.001	<b>0.9243 ± 0.001</b>
CHIMERA	Prostate	<b>0.7663 ± 0.070</b>	0.7605 ± 0.060	0.7368 ± 0.057	0.7184 ± 0.072	0.7394 ± 0.071	<u>0.7657 ± 0.050</u>
<i>Linear Probing (AUC)</i>							
TILS	Breast	0.9822 ± 0.003	0.9788 ± 0.004	0.9819 ± 0.003	<u>0.9827 ± 0.002</u>	0.9782 ± 0.004	<b>0.9838 ± 0.002</b>
TP53	Breast	<u>0.7603 ± 0.052</u>	0.6795 ± 0.054	0.7138 ± 0.070	0.7085 ± 0.076	0.7317 ± 0.066	<b>0.8046 ± 0.048</b>
IDC	Breast	<u>0.9778 ± 0.0008</u>	0.9756 ± 0.001	0.9488 ± 0.002	0.9488 ± 0.002	0.9770 ± 0.0009	<b>0.9796 ± 0.0009</b>
BRCA	Breast	<u>0.8226 ± 0.019</u>	<b>0.8489 ± 0.025</b>	0.7943 ± 0.030	0.7809 ± 0.019	0.8146 ± 0.025	0.8156 ± 0.029
BreakHis (Bin.)*	Breast	0.9578	<u>0.9630</u>	0.9471	0.9415	<b>0.9657</b>	0.9626
BreakHis (Sub.)**	Breast	0.8436	<b>0.8711</b>	0.7653	0.8033	0.8226	<u>0.8465</u>
Gleason	Prostate	<b>0.9846 ± 0.0008</b>	0.9790 ± 0.001	0.9721 ± 0.001	0.9708 ± 0.001	0.9774 ± 0.001	<u>0.9841 ± 0.001</u>
AGGC	Prostate	0.9955 ± 0.0001	<u>0.9956 ± 0.0002</u>	0.9939 ± 0.0002	0.9921 ± 0.0002	0.9951 ± 0.0001	<b>0.9958 ± 0.0002</b>
CHIMERA	Prostate	0.8451 ± 0.090	<b>0.8653 ± 0.106</b>	0.7980 ± 0.092	0.8173 ± 0.081	<u>0.8572 ± 0.079</u>	0.8520 ± 0.103

## Robustness Index

In addition, we quantified robustness of each model against image variations originating from multiple medical centers using the robustness index, following (de Jong, Marcus, and Teuwen 2025). We randomly sampled an equal number of patches ( $= 40$ ) in each of five tissue classes (invasive tumor, in-situ tumor, tumor-associated stroma, inflamed stroma, and necrosis) spanning 21 medical centers in the TIGER dataset (Shephard et al. 2022). We first sampled a query patch, selected the top  $k$  ( $\in 3, 5, 10, 20$ ) nearest neighbor patches of the query, and measured the ratio of tissue consistency over center consistency (i.e., number of neighbor patches with the same tissue / number of neighbor patches with the same center). Therefore, larger robustness index ( $> 1$ ) represents better discrimination of biologically meaningful features than medical centers. We performed five-fold cross-validation for each FM.

## Results

### Feature Similarity Before / After G2L

Table 1 summarizes the feature similarity measured by CKA values between the teacher (H-optimus-0) and student (Hibou-L) models before and after applying the G2L framework. In the BRCA benchmark, the CKA value was substantially increased after G2L (from 0.76 to 0.97), indicating that the student FM captures spatial information in the latent space highly similar to that of the teacher FM. A similar trend was observed in the BreakHis benchmark (e.g., from 0.89 to 0.96 in 40x magnification). Interestingly,

Table 3: Robustness index of foundation models across different  $k$  values. The best index is highlighted in **bold**.

Model	$k = 3$	$k = 5$	$k = 10$	$k = 20$
H-optimus-0	1.0826 ± 0.03	1.1890 ± 0.04	1.3730 ± 0.07	1.8467 ± 0.12
UNI-v2	1.0682 ± 0.03	1.2433 ± 0.05	1.4113 ± 0.05	1.8548 ± 0.10
Virchow	1.0137 ± 0.04	1.1006 ± 0.03	1.1351 ± 0.04	1.2850 ± 0.07
UNI	1.0701 ± 0.04	1.1460 ± 0.02	1.4110 ± 0.04	1.7811 ± 0.07
Hibou-L	0.9056 ± 0.03	0.9905 ± 0.02	1.0879 ± 0.01	1.1855 ± 0.08
G2L (Ours)	<b>1.0891 ± 0.02</b>	<b>1.3002 ± 0.10</b>	<b>1.5021 ± 0.06</b>	<b>2.0316 ± 0.09</b>

the improvement was consistent across magnifications (40x, 100x, 200x, and 400x), suggesting that the G2L framework was successfully applied regardless of magnification scale.

### Downstream Task Benchmark

Table 2 compares the performance of existing FMs and the G2L-distilled FM across different benchmark tasks. In general, the G2L-distilled FM achieved top performance in many benchmarks (TILS, TP53, IDC, and AGGC) and ranked second in others (BreakHis and Gleason), with the exception of BRCA. The original H-optimus-0, which is the largest giga-scale FM in this comparison, also achieved competitive results, ranking first in BreakHis-Binary and Gleason and second in TILS, TP53 and BRCA. In addition, UNI-v2, which is a huge-scale FM, reported the best performance values in BRCA and BreakHis-Subtyping.

The substantial performance gains of the G2L-distilled FM over the others has an important implication: Although

the G2L model has only 15% of the parameters of the giga-scale teacher FM (and 50% parameters compared to the huge-scale models), it demonstrates better representational discrimination in multiple tasks, potentially capturing delicate, cancer-specific morphological features. For example, in the TP53 mutation prediction benchmark, the performance between H-optimus-0 and G2L (0.66 vs. 0.69) suggests that the G2L model can better discriminate subtle morphology-genomics correlations that may be under-represented in the multi-cancer teacher. Similarly, the performance gap in the TILS detection benchmark, although modest, may indicate higher sensitivity of the G2L model to immune-related histological patterns.

### Robustness Index

Table 3 presents the robustness index of different FMs across different number of nearest neighbors ( $k = 3, 5, 10$ , and  $20$ ). The G2L-distilled model consistently surpassed both the teacher and all other models. These results support the clinical applicability of the G2L model, indicating its superior ability to prioritize biologically meaningful features over image variations originating from different institutions.

### Conclusion

In this work, we demonstrated that the high performance of a giga-scale pathology FM can be achieved with a much smaller large-scale FM through efficient knowledge transfer. The proposed G2L framework significantly boosted model performance using only 1K pathology slides, reducing both data and computational demands while achieving giga-scale-level performance. Notably, the G2L-distilled model even outperformed its giga-scale teacher and larger counterparts in many downstream benchmarks. Overall, these findings highlight G2L as a practical and cost-effective method for developing powerful cancer-specific pathology FMs without prohibitive computational resources.

### References

Abousamra, S.; Gupta, R.; Hou, L.; Batiste, R.; Zhao, T.; Shankar, A.; Rao, A.; Chen, C.; Samaras, D.; Kurc, T.; et al. 2022. Deep learning-based mapping of tumor infiltrating lymphocytes in whole slide images of 23 types of cancer. *Frontiers in Oncology*, 11: 806603.

Arvaniti, E.; Fricker, K. S.; Moret, M.; Rupp, N.; Hermanns, T.; Fankhauser, C.; Wey, N.; Wild, P. J.; Rueschoff, J. H.; and Claassen, M. 2018. Automated Gleason grading of prostate cancer tissue microarrays via deep learning. *Scientific Reports*, 8(1).

Brancati, N.; Anniciello, A. M.; Pati, P.; Riccio, D.; Scognamiglio, G.; Jaume, G.; others; and Frucci, M. 2022. Bracs: A dataset for breast carcinoma subtyping in h&e histology images. *Database*, 2022: baac093.

Cappadona, J.; Zeng, K.-G.; Fernandez-Granda, C.; Witowski, J.; LeCun, Y.; and Geras, K. J. 2024. Squeezing performance from pathology foundation models with chained hyperparameter searches. In *NeurIPS 2024 Workshop: Self-Supervised Learning-Theory and Practice*.

Caron, M.; Touvron, H.; Misra, I.; Jégou, H.; Mairal, J.; Bojanowski, P.; and Joulin, A. 2021. Emerging Properties in Self-Supervised Vision Transformers. In *Proceedings of the IEEE/CVF International Conference on Computer Vision (ICCV)*, 9650–9660.

Chen, R. J.; Ding, T.; Lu, M. Y.; Williamson, D. F.; Jaume, G.; Chen, B.; Zhang, A.; Shao, D.; Song, A. H.; Shaban, M.; et al. 2024. Towards a General-Purpose Foundation Model for Computational Pathology. *Nature Medicine*.

Chen, T.; Kornblith, S.; Norouzi, M.; and Hinton, G. 2020. A simple framework for contrastive learning of visual representations. In *International Conference on Machine Learning (ICML)*, 1597–1607. PMLR.

Chia, C.; Spaans, R.; Khoramnia, F.; Faryna, K.; Mohammadiou, M.; Zuiverloon, T.; van Basten, J.-P.; Vermeulen, S.; Litjens, G.; and Khalili, N. 2025. CHIMERA: Combining HIstology, Medical Imaging (Radiology), and molEcular Data for Medical pRognosis and diAgnosis. <https://chimera.grand-challenge.org/>. Accessed: 2025-10-03.

de Jong, E. D.; Marcus, E.; and Teuwen, J. 2025. Current pathology foundation models are unrobust to medical center differences. *arXiv preprint arXiv:2501.18055*.

Ding, T.; Wagner, S. J.; Song, A. H.; Chen, R. J.; Lu, M. Y.; Zhang, A.; Chen, C.; Shaban, M.; Chen, M.; and Mahmood, F. 2025. A multimodal whole-slide foundation model for pathology. *Nature Medicine*, 31(2): 535–547.

Dosovitskiy, A.; Beyer, L.; Kolesnikov, A.; Weissenborn, D.; Zhai, X.; Unterthiner, T.; Dehghani, M.; Minderer, M.; Heigold, G.; Gelly, S.; et al. 2021. An Image Is Worth 16x16 Words: Transformers for Image Recognition at Scale. *International Conference on Learning Representations (ICLR)*. Published as a Conference Paper at ICLR 2021.

Filot, A.; Jacob, P.; A., M. K.; and Saillard, C. 2024. Phikon-v2: A Large and Public Feature Extractor for Biomarker Prediction. *arXiv preprint arXiv:2409.09173*.

He, K.; Chen, X.; Xie, S.; Li, Y.; Dollar, P.; and Girshick, R. 2022. Masked autoencoders are scalable vision learners. In *Proceedings of the IEEE/CVF conference on computer vision and pattern recognition (CVPR)*. CVPR 2022 (optional).

He, K.; Fan, H.; Wu, Y.; Xie, S.; and Girshick, R. 2020. Momentum Contrast for Unsupervised Visual Representation Learning. In *Proceedings of the IEEE/CVF Conference on Computer Vision and Pattern Recognition (CVPR)*, 9729–9738.

Huo, X.; et al. 2022. Comprehensive AI model development for Gleason grading: from scanning, cloud-based annotation to pathologist AI interaction. Preprint at SSRN 4172090.

Janowczyk, A.; and Madabhushi, A. 2016. Deep learning for digital pathology image analysis: A comprehensive tutorial with selected use cases. *Journal of Pathology Informatics*, 7(1).

Kingma, D. P.; and Ba, J. 2015. Adam: A Method for Stochastic Optimization. In *International Conference on Learning Representations (ICLR)*.

Kornblith, S.; Shlens, J.; and Hinton, G. 2019. Similarity of Neural Network Representations Revisited. In *International Conference on Machine Learning (ICML)*.

Lee, S. 2025. Pathology WSI Tile Sampling System. <https://github.com/CocoSungMin/Pathology-WSI-Tile-Sampling-System>. GitHub repository.

Li, J.; Hu, J.; Sun, Q.; Yan, R.; Ouyang, M.; Guan, T.; Li, J.; Zhu, Y.; and He, Y. 2025. Can We Simplify Slide-level Fine-tuning of Pathology Foundation Models? *arXiv preprint arXiv:2502.20823*.

Miles, R.; and Mikolajczyk, K. 2024. Understanding the role of the projector in knowledge distillation. In *Proceedings of the AAAI Conference on Artificial Intelligence*, volume 38, 4233–4241.

Nechaev, D.; Pchelnikov, A.; and Ivanova, E. 2024. Hibou: A family of foundational vision transformers for pathology. *arXiv preprint arXiv:2406.05074*.

Oquab, M.; Darcret, T.; Moutakanni, T.-H. V.; Szafraniec, M.; Khalidov, V.; Fernandez, P.; Haziza, D.; Massa, F.; El-Nouby, A.; Howes, R.; Huang, Y.; Xu, Y. H.; and Li, P. B. 2023. DINOv2: Learning Robust Visual Features without Supervision. *Transactions on Machine Learning Research*.

Qu, H.; Zhou, M.; Yan, Z.; Wang, H.; Rustgi, V. K.; Zhang, S.; others; and Metaxas, D. N. 2021. Genetic mutation and biological pathway prediction based on whole slide images in breast carcinoma using deep learning. *NPJ Precision Oncology*, 5(1): 87.

Saillard, C.; Jenatton, R.; Llinares-López, F.; Mariet, Z.; Cahané, D.; Durand, E.; and Vert, J. 2024. H-optimus-0. <https://github.com/bioptimus/releases/tree/main/models/h-optimus/v0>. Version 0, GitHub Repository.

Saltz, J.; Gupta, R.; Hou, L.; Kurc, T.; Singh, P.; Nguyen, V.; others; and Danilova, L. 2018. Spatial organization and molecular correlation of tumor-infiltrating lymphocytes using deep learning on pathology images. *Cell Reports*, 23(1): 181–193.

Shephard, A.; Jahanifar, M.; Wang, R.; Dawood, M.; Graham, S.; Sidlauskas, K.; others; and Raza, S. E. A. 2022. Tiager: Tumor-infiltrating lymphocyte scoring in breast cancer for the tiger challenge. *arXiv preprint arXiv:2206.11943*.

Spanhol, F. A.; Oliveira, L. S.; Petitjean, C.; and Heutte, L. 2015. A Dataset for Breast Cancer Histopathological Image Classification. *IEEE Transactions on Biomedical Engineering*, 63(7).

Vorontsov, E.; Bozkurt, A.; Casson, A.; Shaikovski, G.; Zelechowski, M.; Liu, S.; others; and Fuchs, T. J. 2023. Virchow: A million-slide digital pathology foundation model. *arXiv preprint arXiv:2309.07778*.

Weigelt, B.; Geyer, F. C.; and Reis-Filho, J. S. 2010. Histological types of breast cancer: How special are they? *Molecular Oncology*, 4(3): 192–208.

Weinstein, J. N.; Collisson, E. A.; Mills, G. B.; Shaw, K. R.; Ozenberger, B. A.; Ellrott, K.; Shmulevich, I.; Sander, C.; and Stuart, J. M. 2013. The Cancer Genome Atlas Pan-Cancer Analysis Project. *Nature Genetics*, 45(10): 1113–1120.

Xu, H.; Usuyama, N.; Bagga, J.; Zhang, S.; Rao, R.; Naumann, T.; others; and Poon, H. 2024. A whole-slide foundation model for digital pathology from real-world data. *Nature*, 630(8015): 181–188.

Zhao, J.; Lin, S.-Y.; Attias, R.; Mathews, L.; Engel, C.; Larghero, G.; others; and Yu, K.-H. 2025. Uncertainty-aware ensemble of foundation models differentiates glioblastoma from its mimics. *Nature Communications*, 16(1): 8341.

Zhou, J.; Wei, C.; Wang, H.; Shen, W.; Xie, C.; Yuille, A.; and Kong, T. 2022. iBoT: Image BERT Pre-training with Online Tokenizer. In *International Conference on Learning Representations. ICLR 2022 (optional)*.

Zimmermann, E.; Vorontsov, E.; Viret, J.; Casson, A.; Zelechowski, M.; Shaikovski, G.; Tenenholz, N.; Hall, J.; Klimstra, D.; Yousfi, R.; Fuchs, T.; Fusi, N.; Liu, S.; and Seversen, K. 2024. Virchow2: Scaling Self-Supervised Mixed Magnification Models in Pathology. *arXiv preprint arXiv:2408.00738*.